Performance of an Optical COTS Station for the wide-field Detection of Resident Space Objects

Thomas Delaite

Jocelyn Couetdic, Éric Glemet, Frederic Cassaing
DTIS, Onera

Abstract

Space Situational Awareness (SSA) becomes more critical as space gets more and more congested. Following the successful development of the GRAVES radar for LEO satellites, Onera is considering an optical ground station to track Resident Space Objects (RSOs), targeted primarily for altitudes above 2,000 km. Two main approaches are reported in the literature: streak detection in single long exposure frames and Track-before-Detect (TBD) algorithms applied to image stacks. The recent availability of efficient components like sCMOS cameras and GPUs makes on-the-fly TBD a realistic and affordable solution.

Our objective is to specify, optimize, integrate and validate the most efficient hardware and software components for a prototype ground station, ensuring optimal performance and reliability of the system. The performance of the system needs to be characterized to enable future orbit determination.

The first step of the workflow involves a detection algorithm based on a TBD method, which belongs to a class of tracking methods operating directly on raw temporal series of images. The proposed adapted version, inspired by exoplanet detection research, simultaneously estimates the position and velocity of faint satellites with high accuracy. While this approach typically demands increased computational power for real-time processing of incoming image data, the high acquisition frequency leads to simple motion and shape of the objects in the image, resulting in a fast and efficient algorithm. Furthermore, the resultant algorithm exhibits high parallelizability, leading to a considerable reduction in computation time through its implementation on GPUs.

The second step involves the accurate projection of the true state of an observed object into the measurement space. Achieving this requires precise temporal stamping of the data, which must account for the camera's reading mode. Plate solving is used to compute the projection function that maps pixels to the sky. Conventional methods from astronomy need to be analyzed and adapted to meet SSA requirements.

Finally, an extensive measurement campaign was performed to explore the performance of the system with on-sky data. The system accuracy is analysed in terms of residuals between our measurements and the projection of calibration satellites' states. Therefore, the analysis not only measures our detection accuracy, but the overall capacity of the system to track RSOs. It demonstrates sub-arcsecond precision in position and under the arcsecond per second in velocity. An emphasis is put on obtaining residuals over the full range of observations parameters. This allowed to highlight, for example, an increase in the error at low altitude. In addition, the system's empirical performance in low SNR conditions are investigated on faint objects taking advantage of the satellites' passage into eclipse. This characterisation of a reliable error model is the key to future orbit determination.

1. CONTEXT

In order to extend its expertise built up over many years on low Earth orbit with the GRAVES radar [1], Onera currently completes the development of a robotic optical station. Installed in May 2022 in its Palaiseau center for integration, CICLOPE should be relocated in 2024 in a better place. The current instrumentation is intended to address detection and orbit determination of objects on medium to high Earth orbits, characterization (through photometric analysis or low-resolution spectroscopy), or innovative imaging methods [2]. The station includes a Celestron® RASA 14 tube completed by Astelco® with a NTM-500 mount, a filter selector, a completely retractable enclosure and a Boltwood® II cloud sensor; a Miratlas® ISM including a full-sky camera; a cooled 6K×6K backside-illuminated sCMOS camera with 10 um pitch coupled to a DELL® Linux server with 3 Nvidia® GPU. The camera just covers the 60 mm diameter linear field from the tube, providing a 2.6 arcsec/pix scale over a 4.3°×4.3° angular field. The main objective of the prototyping phase, presented in this document, is to characterize both the detection capability and the precision of our system hardware and software, using real data.

The paper organization follows the main steps of the prototyping workflow depicted in Fig. 1. First, we develop the process used to detect resident space object (RSO) in temporal series of sky images. Then, we detail the direct projection of a RSO state into the measurement space, which is crucial to initiate orbit restitution. Finally, we present the results obtained on the observation of multiple GNSS satellites. The analysis of the residuals is conducted to quantify the bias and variance, and determine their potential source.
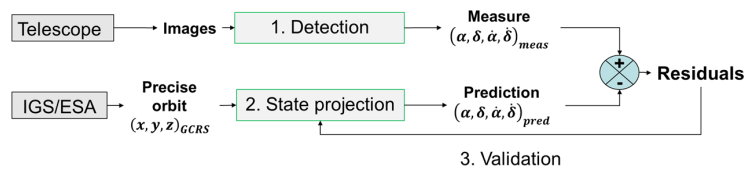

Figure 1: General workflow of prototyping.

## 2.   METHOD FOR SATELLITE DETECTION

Several methods have been proposed to tackle the RSO detection with ground-based optical sensors. The primary approaches include streak-detection, particles, and shift-and-add methods. Streak detection relies on segment detection algorithm and work with single long-exposure images. While very fast and efficient for any orbital regime, a part of the signal-to-noise ratio is lost because during the integration time, the RSO shift dilutes the useful signal over several pixels while background noise is continuously integrated. Sequential method (Multi-Bernoulli [3][4], particle algorithms [5]) show very good results and converge faster than shift-add method [6]. However, we found that there is no consistent model for the intensity evolution of all satellites. Fig. 2 shows two special cases, a vanishing satellite (Fig. 2a) a priori due to atmospheric conditions, and a flashing satellite (Fig. 2b). The short-term light curve, presented in Fig. 3 over a 10 seconds time-lapse and confirmed in individual frames, shows a common periodic behavior where the satellite turns black for several frames between peaks. A sequential processing is likely to trigger multiple detections, or will need special care for many special cases to fuse those detections. A global stacking method allows us to ignore any irregular fluctuation.

We develop here an adapted shift-and-add like algorithm that we introduced in [7], that is able to estimate the position and velocity of RSOs in temporal series of telescope images.

The ground station is initially designed to target RSO population in MEO orbit. Introducing the Earth standard gravitational parameter μ, the satellite speed V_{sat}, apparent angular velocity $\omega_{sat/obs}$ and elevation h_{sat} verify for circular orbit at zenith

$$V_{sat} = \omega_{sat/earth} * (R_{earth} + h_{sat}) = \omega_{sat/obs} * h_{sat} = \sqrt{\frac{\mu}{(R_{earth} + h_{sat})}} \tag{1}$$

For GNSS satellites, solving Eq. 1 for the apparent angular speed leads to an angular speed of up to 40 arcsec/s, corresponding to 15 pixels/s.
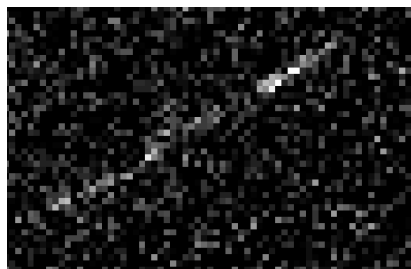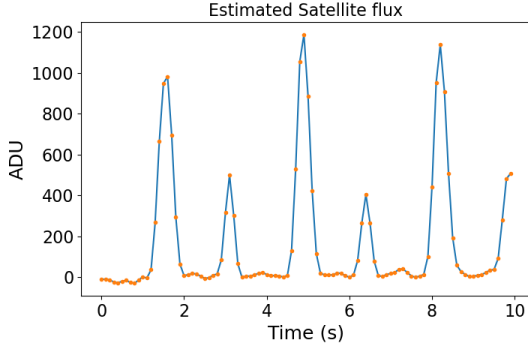

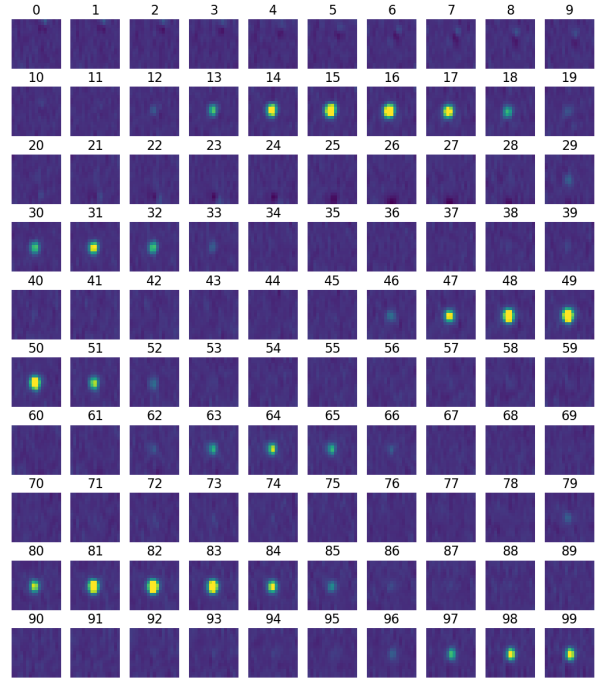(a) Temporary vanishing satellite at low elevation (NAVSTAR 54).
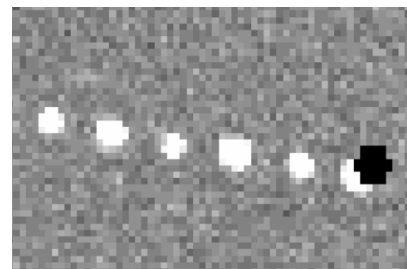
(b) Flashing satellite (PALABA 4B).

Figure 2: Synthetic long-exposure frames (cf I_{max} hereafter) of satellites with highly varying intensities. Background and stars (black points) have been removed.

Estimated Satellite flux

(a) Light curve sampled at 20 Hz.

(b) Flashing satellite sequence, using detection to register the images. Processed frames (after master bias, flat, background removal, and adapted filter) recorded at 10 Hz.

Figure 3: Temporal and spatial behavior of a flashing satellite (the GEO satellite PALABA 4B).

2.1 Target Model

We first develop a simple model for the light distribution of RSOs, assuming we work with a sequence of images $I(.,k)$ timestamped $T(k)$ (time of the k-th frame relative to an arbitrary origin T_0). The fraction of light on pixel at $\boldsymbol{p} = (x,y)$ at time $T(k)$ of an object with position $\boldsymbol{p_0}$ at T_0 and velocity $\boldsymbol{v}$ is noted $s(\boldsymbol{p}, T(k) \; ; \; \boldsymbol{p_0}, \boldsymbol{v})$.

The shape or light distribution $s(\boldsymbol{p}, T(k) \; ; \; \boldsymbol{p_0}, \boldsymbol{0})$ of a static object at position $\boldsymbol{p}$ in frame $I(.,k)$, i.e. the PSF if we assume all RSOs to be unresolved, can be modelled as a Gaussian with width equal to the seeing, estimated on stars. Also, with enough data, an experimental effective PSF map can be integrated and replace the s function. Assuming that the exposure time T_{expo} is short enough compared to the characteristic time it takes for a satellite to move along one pixel, i.e. $T_{pix} = \theta_{pix}/||\boldsymbol{v}||$, the light distribution is then just

$$s(\boldsymbol{p}, T(k) \; ; \; \boldsymbol{p_0}, \boldsymbol{v}) = PSF(\boldsymbol{p}, T(k) \; ; \; \boldsymbol{p_0}) \quad \text{if} \quad ||\boldsymbol{v}|| < V_{max}. \tag{2}$$

The main assumption is that the light spatial distribution is independent of the satellite velocity, meaning a single kernel is sufficient to cover all hypothesis, thus drastically reducing the computing time. The maximum velocity V_{max} for which this hypothesis holds is dependent on the acquisition frequency.

Over a short total exposure (less than a few tens of seconds), we use the classic assumption that the RSO has a constant velocity in the pixel space. This translates as the following equation

$$s(\boldsymbol{p}, T(k) \; ; \; \boldsymbol{p_0}, \boldsymbol{v}) = s(\boldsymbol{p} - \boldsymbol{p_0} - \boldsymbol{v}T(k), T(k) \; ; \; \boldsymbol{0}, \boldsymbol{0}). \tag{3}$$

The actual image in one frame of each object is its shape multiplied by its mean intensity $A_i(k)$ over the exposure time. Each image sequence $I(\cdot,k)$ is always acquired with the telescope in sidereal tracking mode. After calibration, the images model can be written as

$$I(\boldsymbol{p},k) = \sum_i A_i(T(k)) s(\boldsymbol{p}, T(k); \boldsymbol{p}_{0,i}, \boldsymbol{v}_i) + BG(\boldsymbol{p}, T(k)) + n(\boldsymbol{p}, T(k)), \tag{4}$$

where the residual noise n, mainly composed of the photon and detector noises, is assumed to be white and Gaussian. BG is the background, composed of stars, diffuse light, and other stationary sources.

2.2 Data and Pre-processing

The first step of the data processing consists in the classical removal of the master bias, bad (hot, defective or non-linear) pixels and flattening of the raw images, which is already assumed in Eq. 4.

From the temporal series, the median and maximum image are computed as

$$I_{max}(\boldsymbol{p}) = \max_k(I(\boldsymbol{p},k)), \qquad\qquad I_{median}(\boldsymbol{p}) = \operatorname{med}_k(I(\boldsymbol{p},k)). \tag{5}$$

The maximum image I_{max} is used to create 2-dimensional images for illustration purpose, such as in Fig. 2.

Because the telescope is in sidereal tracking mode, and the researched objects are moving, the median image is an estimator of the background

$$BG(r,k) \approx I_{median}(r), \tag{6}$$

which is removed from each frame.

The background estimation is used to compute a star mask. Stationary sources, such as stars, are detected and removed through a sigma clipping on the median image. A morphological filter is applied to the mask to eliminate star residuals due to the telescope tracking errors and atmospheric tilt.

Finally, the pixel noise map $\sigma_I(x,y)$ is computed using the read-noise σ_{read} estimated as the standard deviation of the sequence used for the master bias frame, and the median image as the mean of the shot noise (for camera gain of 1). The noise map σ_I is forced to infinite at the location of stars and defective pixels. For programming purpose, we actually set the inverse variance map σ_I^{-2} to zero.

$$\sigma_I^2(x,y) = \sigma_{read}^2(x,y) + I_{median}(x,y),$$
$$\sigma_I^{-2}(mask) = 0. \tag{7}$$

2.3 Exposure time

The signal-to-noise ratio (SNR) per frame is maximized by minimizing the integrated background per pixel by setting the exposure close to the satellite pixel-crossing time. An analytic formula for the exposure time T_{opt} that maximizes the SNR can be derived as a function of the target pixel time T_{pix}, the light spread σ_{PSF}, the read noise σ_{read} and the background noise σ_{bg} according to:

$$T_{opt} \simeq T_{pix} \frac{\sigma_{read}}{\sigma_{bg}} \sqrt{2\sigma_{PSF}}, \tag{8}$$

which yields similar results as the sensitivity curve for the Space Surveillance Telescope (SST) [8, fig. 8]. The trade-off between an optimal exposure time, the diverse target velocities and the point-shape assumption will be developed in a forthcoming paper.

2.4 Likelihood computation

The detection algorithm is similar to the "synthetic tracking" stacking method for near-earth objects (NEO) and RSO detection proposed in [9], [10], but including additional knowledge, as done with the ANDROMEDA method used for exoplanet detection [11]. Under the assumption that the noise is white and Gaussian, it can be shown that maximizing the likelihood ratio of a single target's parameters, $\mathbf{p_0}$ and $\mathbf{v}$, is equivalent to maximizing:

$$\hat{r}_{S/N}(\boldsymbol{p}_0,\boldsymbol{v}) = \frac{\sum_{k,\boldsymbol{p}} \frac{I(\boldsymbol{p},k)\,s(\boldsymbol{p},k;\boldsymbol{p}_0,\boldsymbol{v})}{\sigma_I^2(\boldsymbol{p},k)}}{\left(\sum_{k,\boldsymbol{p}} \frac{s^2(\boldsymbol{p},k;\boldsymbol{p}_0,\boldsymbol{v})}{\sigma_I^2(\boldsymbol{p},k)}\right)^{\frac{1}{2}}}. \tag{9}$$

which is written $\hat{r}_{S/N}$, as it is an estimator of the true SNR of the mean intensity estimator.

Using the assumption under Eq. (2) that the light distribution s is independent of the velocity hypothesis, the cross-correlation (equivalent to a spatial adapted filter) of the images and object model is computed once for every velocity hypothesis:

$$I_{corr}(\boldsymbol{p},k) = \sum_{\boldsymbol{p'}} \frac{s(\boldsymbol{p'},k;\boldsymbol{p},0)\,I(\boldsymbol{p'},k)}{\sigma_I^2(\boldsymbol{p'},k)}, \qquad\qquad \sigma_{corr}^2(\boldsymbol{p},k) = \left(\sum_{\boldsymbol{p'}} \frac{s^2(\boldsymbol{p'},k;\boldsymbol{p},0)}{\sigma_I^2(\boldsymbol{p'},k)}\right) \qquad (10)$$

Injecting the assumption of rectilinear motion from Eq. (3), it can be shown that the maximization of the marginalized likelihood ratio is equivalent to maximizing

$$\hat{r}_{s/b}(\boldsymbol{p_0},\boldsymbol{v}) = \frac{\sum_k I_{corr}(\boldsymbol{p_0}+k\boldsymbol{v}T,k)}{\sqrt{\sum_k \sigma_{corr}(\boldsymbol{p},k)}}. \qquad (11)$$

Which is just a shifted-sum of the correlated images weighted by the noise. Finally, a detection is decided if the likelihood ratio is greater than some threshold τ. The choice of the threshold is up to the user, often as a function of the false alarm rate, and is discussed in [6][9].

2.5 Faster targets / limiting velocity

One of the algorithm speedup comes from the assumptions that all targets have the same shape s, regardless of their velocity. But, obviously, satellites faster than the acquisition frequency will form streaks.

The maximum speed that we can optimally detect is mainly limited by hardware. Our camera read-out in full frame (6K×6K) fastest frequency is $f_{max} = 50$ Hz. We found that the proposed method is still efficient up to RSO apparent velocity of 2 pixel/frame. At 50 Hz, with 2.6 arcsec/pixel, it corresponds to an angular velocity of $\omega_{max} = v f_{max} \theta_{pix} = 250"/s$.

Solving Eq. (1) for h at ω_{max} gives a maximum elevation of 3 000 km, corresponding to most of the MEO range, for the method to stay optimal. In practice, detections are still correct for faster targets, up to a few pixels per frame, but without an optimal SNR.

2.6 Likelihood reduction and output detections

The likelihood equation holds for a single satellites. We first assume the –most likely– case of an isolated satellite. The $\hat{r}_{s/b}$ function should present values over the threshold for parameters at and around the true $(\boldsymbol{p_0},\boldsymbol{v})$, but only the local maximum needs to be retrieved. A sub-pixel maxima can thus be found by fitting a polynomial.

The likelihood map can also be used for multiple detection. The minimum separation for two satellites to be detected is in the order of the seeing θ_0 in the position space, and θ_0/T_{expo} in the velocity space. The proposed method is thus able to separate two satellites as soon as at least one of the four coordinates involved sufficiently differ from these limits.

The algorithm uses relative time between frames, but a time reference needs to be chosen along with $(\boldsymbol{p_0},\boldsymbol{v})$ parameters, which is chosen as the mean time of the exposures. The exposure time has to be taken into account: with an exposure of T_{expo} and a reference time T_0, the centroid is the position of the satellite at $T_0 + T_{expo}/2$.

Last, the detected positions and velocities are used to extract the sequence sub-cubes, such as the one shown in Fig. 3, for further processing.

3. STATE PROJECTION

Even if the detection algorithm can provide milli-pixel accuracy, its usefulness is limited if we cannot precisely associate the detections with the satellite state. Here, a direct model M (or measure function) is developed from state to measure. This model will be valuable for solving the inverse problem from measure to state and refining the orbital parameters in the future.

For demonstration and quantification purpose, we chose the celestial frame as the common comparison space. Thus, detection in pixels, and satellite state, originally in an earth fixed frame (ITRF), are projected into the celestial apparent position (ICRF), to express residuals in this more perceivable space.

Our goal is to accurately compute the predicted apparent position and velocity $(\alpha, \delta, \dot{\alpha}, \dot{\delta})_{pred} = proj(r_{rso}, \dot{r}_{rso}, T_{obs})$. On the other hand, it is to compute the corresponding sky position and velocity of the measured pixel position and velocity $(\alpha, \delta, \dot{\alpha}, \dot{\delta})_{obs}$ from the detection outputs $(\boldsymbol{p}_0, \boldsymbol{v}, T_{obs})$.

3.1 Astrometry, pixel to sky transformation

Using reference stars with known positions from a catalog, we can interpolate the apparent line-of-sight vector of an unknown source, in the chosen catalog reference frame. The method consists in fitting a transformation $A : (x, y) \rightarrow (\alpha, \delta)$ that computes the apparent ICRS (if the input catalog is given in ICRS) position of pixel positions, using a set of known matches $(x, y)_I \leftrightarrow (\alpha, \delta)_{cat}$. Only three matches are needed to get a linear solution, but usually we use more pixel-star matches to fit the transformation with a higher order polynomial through a least-square minimization. Our reference catalog is a made from Gaia DR3 [12], from the European Space Agency (ESA) mission Gaia [13]. Using given proper motions, we are able to compute an up-to-date catalog for the dates of observation.

The astrometry.net software [14], [15] offers a great and complete solution to get a first solution for the pixel to sky transformation, along with the set of matches used for the estimation. Astrometry.net can provide an optional polynomial correction to correct for the different distortions that make the sky to image projection diverge from a simple orthoscopic projection. Since our tube has revolution symmetry, we can expect its distortion to be efficiently quantified by a single Seidel coefficient (S_V or W_{311}), leading to a 3rd order polynomial correction. Our distortion amounts to up to 5 arcsec at the border of the image.

The correction also has to account for external distortions, which are caused by non-homogeneous deformations of the apparent position of the star. The two main components are atmospheric differential refraction (up to more than 100 arcseconds for 4° field at 10° elevation [16], maximum at 0° elevation) and differential light aberration (up to a few arcsec, maximum in the direction of the earth apex and antiapex).

The variance of the astrometric reduction is estimated as the empirical variance using the set of pixel to $(\alpha, \delta)_{cat}$ association. In our dataset, the mean variance is in the order of a few hundredths of arcseconds. Which means that further work is needed to improve the transformation.

This may come from the coupling between the wide field and observed spectral bandwidth which leads to high chromatic aberration, that we plan to address. The high number of stars available, due to the wide field of view and the high sensitivity, should allow us to select a reduced set of stars which will reduce differential chromatic aberration and astrometric errors. Assuming that RSOs have a spectrum similar to that of the sun, we can select a list of reference stars from their spectral type, given in modern catalogs.

A is applied to each detected coordinates $\boldsymbol{p}_0 = (x_0, y_0)$ to get a list of sky positions $(\alpha, \delta)_{obs}$. The apparent velocity $(\dot{\alpha}, \dot{\delta})_{obs}$ is computed by finite difference, using the estimated pixel velocity $\boldsymbol{v}$.

3.2 RSO predicted apparent sky position

Initial dating of each frame   Modern cameras include an internal timer with microsecond accuracy. Each frame k start exposure is timestamped $T_{cam}(k)$ corresponding to seconds from the timer initial date $T0_{UTC}$.

For each observation (sequence of images), we query the camera timestamps along with the system timestamps (UTC date synchronized through NTP). Each query is sequential (so not simultaneous) but only take several nanoseconds, so one query should suffice to get a good enough mapping between camera and UTC clocks. To verify the linearity of the internal camera clock, UTC and camera time are taken before and after acquisition and the time differences are verified to be approximately equal. We found a difference less than a few nanoseconds, under our measurement precision capacity.

The actual measurement date $T_{obs}(k)$ of a frame k is taken as the frame date plus half the exposure time. Assuming linear motion, it corresponds to the date when the satellite pixel position is the centroid of its integrated shape over the exposure, which is the expected output of the detection algorithm. The reference UTC date for each frame is then:

$$T_{obs}(k) = T0_{UTC} + T_{cam}(k) + \frac{T_{expo}}{2}. \tag{12}$$

The analysis of residuals on calibration satellites over a long time should indicate if this timing method introduces systematic bias.

Light time delay   The satellite apparent position differs from its geometrical position (true position at the instant of measure) due to the finite speed of light. The light time correction accounts for 2 arcsec for a GEO orbit, and up to 5 arcseconds for low orbit (400 km) satellites. A classic iterative algorithm is used to find the light time delay δt_{lt}. The observed position of the object at T_{obs} is then the RSO position $\boldsymbol{r}_{rso}$ at $T_{obs} - \Delta t$.

Rolling Shutter Correction   Our camera uses a rolling shutter, which adds distortion to the image when used on dynamic scenes.

The camera line delay in given to be 7.8 µs for the imaging mode used in production. For a satellite travelling 100 pixels during the 10 seconds sequence, the maximal time distortion between both end of the tracklet is in the order of 0,1 ms. We therefore assume that locally the rolling shutter effect is negligible. However, the measure time has to be corrected w.r.t. to the time of the first line, which is given by the internal camera clock. Indeed, for a wide camera with 6K pixels the time difference between the first and last line is 20 ms, which is not negligible.

While not written explicitly after for simplicity, a correction term Δt_{rs} is embedded in the T_{obs} value. It is computed by first projecting the object state into the pixel space using the initial $T_{obs} - \Delta t_{lt}$ to get the predicted line position y_{rso}. The rolling shutter delay Δt_{rs} could be computed through an iterative solution similar to the light time delay correction. In practice, a single iteration is sufficient and we take $\Delta t_{rs} = y_{rso} \times line\_delay$.

If one does not trust or want to verify the line delay given by the camera supplier, a minimization of the residuals w.r.t. to the measure date should show a correlation with the Y-axis pixel coordinates of the image (or the X-axis of the camera if it is read column by column), with a slope corresponding to the line delay. Performing this analysis gave us a compliant value (10% departure from the specified value, using data described in section 4).

Spatial correction   The measure will be given in a celestial frame relative to stars, therefore one has to take into account light aberrations that affect stars but not the satellite, so only annual aberration is taken into account. We invert the light aberration at the position of the object r_{rso} to get its apparent position among the stars.

Velocity projection   The overall projection is a non-linear function of time and observer position. Thus, we chose to estimate the apparent velocity $(\dot{\alpha}, \dot{\delta})_{pred}$ by finite difference of predicted positions.

4.   VALIDATION

In order to validate our detection, but more importantly to characterize the bias and variance of the overall process, ground truth data from calibration satellite states is used. The data we used is mainly retrieved from the Center for Orbit Determination in Europe (CODE) [17], as it offers ephemeris for almost all GNSS constellations. CODE also provides both observed and predicted (future) satellite position, which allow us to precisely point at our selected targets during observation campaigns.

4.1 GNSS data

Interpolation   The GNSS position is provided as ephemeris with a temporal resolution of 5 minutes. To estimate the satellite's state at any date and time, we use spline interpolation.

The ephemeris are provided in an International Terrestrial Reference Frame (ITRF). However GNSS orbits exhibit greater smoothness, thus lower interpolation errors, in the inertial Geocentric Celestial Reference Frame (GCRF). Moreover, the GCRS position is just a step away from the catalogs reference frame.

The accuracy of the interpolation of the ephemeris using splines has been checked by downsampling ephemeris from 5-minutes to 15-minutes, constructing an interpolator from the downsampled ephemeris and computing the difference with the original 5-minutes ephemeris at the sample points. We found a maximum error of 20 cm, which corresponds to 2 mas at 20 000 km, which is negligible compared to the obtained precision of a few hundred mas. Therefore, the interpolated GNSS data are taken as the ground truth for the satellites states.

Observation - measure association   Even if we point toward the target GNSS, multiple detections might occur, so the projected state (prediction) is associated with the nearest neighbor detection (measure). The distance between a measure and the projection is taken as their angular distance, ignoring velocity for now.

The sparsity of the RSO distribution, in relation to the precision of our measurements, which are on the order of a few hundred milliarcseconds, results in an extremely low probability of false associations. Furthermore, GNSS satellites do not exhibit any known companions that might introduce systematic errors to our residual measurements.

The set of measure-prediction association is then filtered, to keep only 'true positive'. If the prediction to nearest detection residual is less than a certain threshold, it is considered a true positive. Obviously, if detections are made all over the parameters space, the detection rate would be 100%. Therefore, a true positive is decided if one and only one detection has a residual of less than 10 arcsec in position and 3 arcsec/s in velocity, then the residual is accounted as an actual residual. Those values are chosen low enough such that it is very unlikely that a false association is made with a close-by object, but high enough compared to our precision such that we don't artificially improve our empirical precision. The average PSF width is 2 pixels, so excluding associations over 10 arcseconds should not artificially improve our precision.

4.2 Observation campaign

We conducted observations of multiple GNSS satellites (5 here) over several nights to obtain measurements with a variety of observation parameters. A set of visible satellites was selected and regularly observed. The telescope is pointed toward the predicted position and image sequences are taken.

The acquisition parameters were:

- 50 ms exposure per frame.

- 100 frames per sequence. It is a trade-off between signal accumulation, computing time and available memory.

The detection algorithm is implemented in CUDA and runs on an A40 GPU. The velocity parameter space is sampled with a 1.5 arcsec/s spacing, and the position space with a 1 pixel spacing (2,6 arcsec).

4.3 State estimation precision

One of the key objectives in the prototyping is to explore potential correlations between residuals and observation parameters such as the elevation, azimuth, Earth velocity to line-of-sight angle, right ascension, declination, X and Y pixel coordinates of the measurements, etc. By incorporating a wide range of measurements, these correlations can be identified and included in the noise model, or lead the user to appropriate corrections.

Position residuals   In figure 4, the histogram of around 1000 residuals projected on the ra-dec (ICRF) axes are shown. We found no per-satellite specific bias, thus all observations are analysed as a whole. In the celestial axes, residuals show a negligible systematic bias, and a standard-deviation of 250 milliarcsec in both angular directions. In this projection, we find a desired non-biased, Gaussian shaped distribution, that enables our result to be integrated in orbit restitution algorithms. This corresponds to a $0, 1$ pixel error, which is commonly taken as a basis for the expected error for centroid estimation algorithms, and is comparable to some high-precision astrometric measurements obtained on GEO satellites, with better sampling (1 arcsec/pixel) and in satellite tracking mode [18].

However, by projecting into the azimuth-elevation frame, the residuals plotted on Fig. 5 present a notable increase trend in the elevation bias at low elevations, while the azimuth estimation stays unbiased, leading us to think that the high bias at low elevation is due to atmospheric effect. It may come from badly corrected differential refraction along with a lack of proper astrometric reference stars in the lower elevation part of the images. Other atmospheric effects are to be investigated. More observations are needed to confirm the trend, especially we need to confirm the trend for objects in other orbital regimes. It can be noted that we are able to detect satellite at the lowest elevations for our site, where the view is obstructed by trees and building under 4°. The decrease in precision with elevation is due to the decrease in SNR for both the satellite (detection precision loss) and the stars (astrometric reduction precision loss) which is explained by an increase in atmospheric extinction.

Although, for SSA application, it is questionable to even observe under 10° elevation. However, this effects seem to be the next wall limiting our precision.
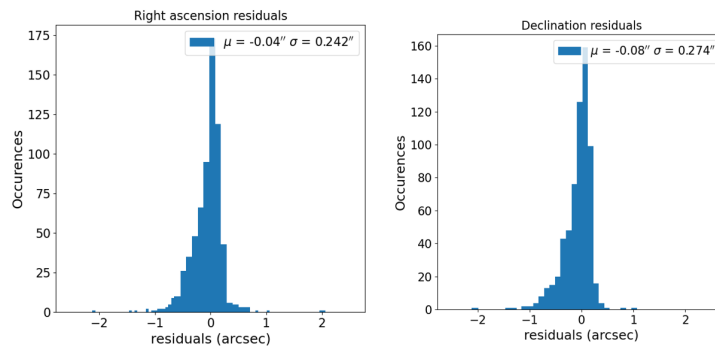
Figure 4: Right ascension and declination residuals between our observations and GNSS projection (800 points).
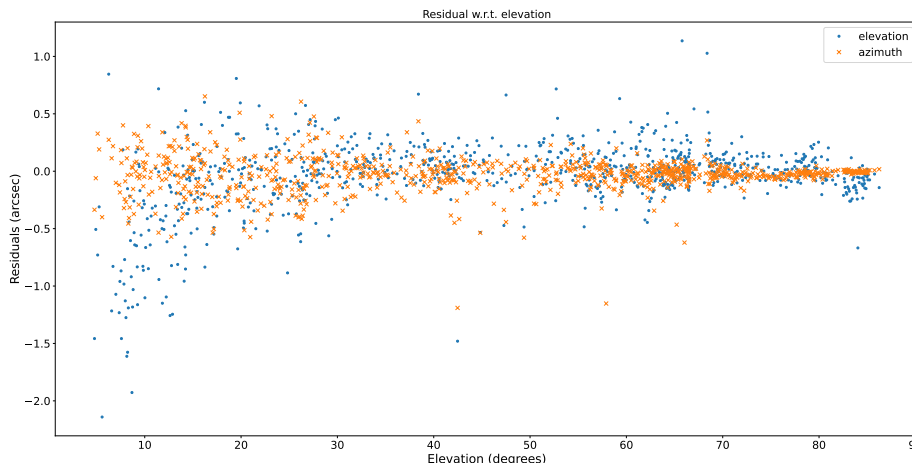

Figure 5: Elevation (blue) and azimuth (orange) residuals w.r.t. elevation. 800 observations of 5 different GPS satellites.

Velocity estimation   The velocity parameter space has been discretized with a 1,5 arcsec/s step, equivalent to a step of 0.6 pixels per second. The residuals histograms in the celestial frame are shown in Fig. 6. We found no systematic bias, and a standard deviation of 340 milliarcsec/s in each direction. Contrary to the position residuals, there is no evidence for a correlation w.r.t. to the elevation, which is to be expected as the bias is cancelled through differentiation. To the authors' knowledge, no comparable velocity estimation analysis have been found in the literature.

4.4 Limiting Magnitude

The knowledge of satellite position allows the validation of very-low SNR detection. We propose a consistent method to estimate the experimental limiting magnitude of our system.

GNSS satellite are much brighter than detection limit. In order to observe faint GNSS, we observed their eclipse, when the satellite travel through the earth shadow. The GPS satellite NAVSTAR 74 eclipse was observed during the nights of 16 and 30 January 2023, its relative flux is shown in Fig. 7. Although the telescope is pointed in the right direction by the ephemeris knowledge, the detection algorithm is not aware of this. Fig. 7 plots the flux associated with the closest detection from the expected position. In addition, points are labelled as true detection (orange disk) only when the angular error is less than 3 arcsec and the velocity error is less than 1 arcsec/s, making it very unlikely that the actual detection corresponds to a wrong detection with this four-dimensional constraint. Otherwise, we mark with a red-cross the dates of observation when we were not able to detect the satellite, despite its presence in the field of view.

We found that we can follow and detect a target with a flux that goes from 1 to 0,01 of it's flux before the eclipse. The detection threshold had to be set very low, increasing the false alarm rate higher than a typical SSA system 'in
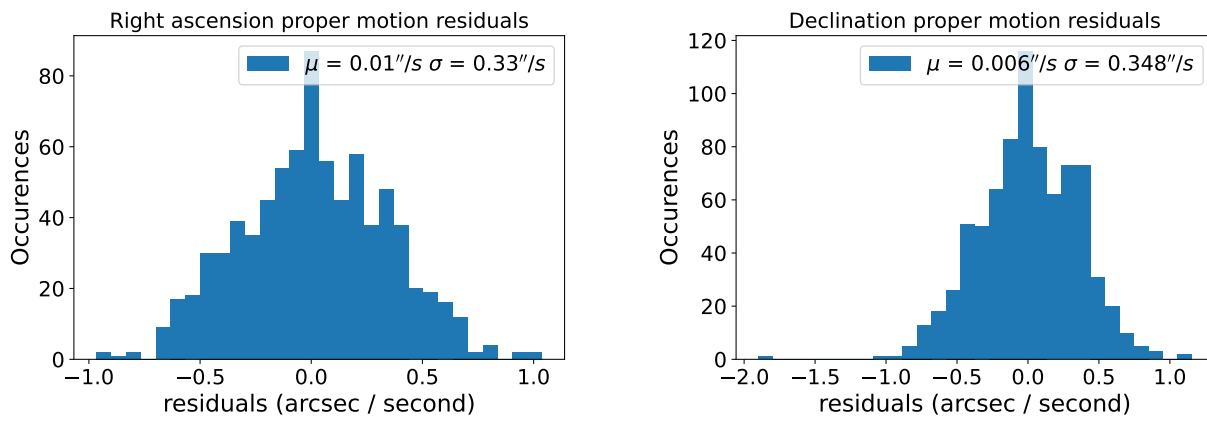
(a) Right ascension proper motion residuals.

(b) Declination proper motion residuals.
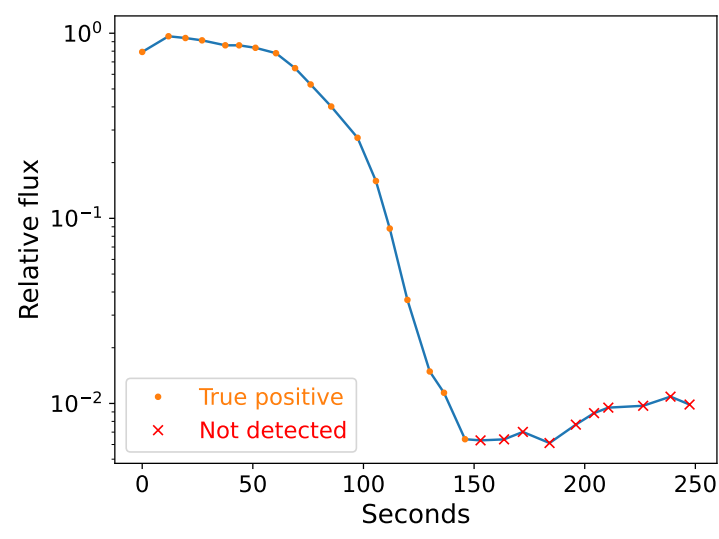
Figure 6: Proper motion residuals.

Figure 7: Flux evolution and detection during eclipse of NAVSTAR 74. Seconds starting from 23h07 on the 16th of January 2023. Red crosses indicate that a sequence pointing the satellite was taken, but no detection was validated.

production' would tolerate. However, it demonstrates the capability of a small telescope to detect very faint objects, using adapted software.

5. CONCLUSION

In this work, we developed the global process of detection and state projection using an optical ground station, which are the basis of Space Surveillance and Tracking. Our residuals show promising results, with an astrometric dispersion about 250 miliarseconds, which is equivalent to or better than some of the best results found in the literature [18]. In addition, the extraction of data cubelets around the satellite tracklet opens the door to SSA through refined processing (close-objects separation, temporal light analysis).

The proposed approach combine precision and magnitude limit considerations with a large field of view, while incorporating a streamlined on-the-fly processing approach. We show consistent results from measurement of multiple satellites. Still, the state projection involves a number of factor that are not easy to model or quantify. The combina-

tion of the non-linear process of time correction, astrometry and others make the whole transformation self-convoluted. Especially, The missing part of the model for low elevation is still to be investigated.

Finally, we presented an easy solution to estimate the limiting magnitude of any RSO detection system, using eclipse. We demonstrated the ability of our method to detect very faint satellite.

The characterisation of the whole chain, in terms of precision and dispersion, should now allow us to integrate our measurements in an orbit determination system.

6. ACKNOWLEDGMENTS

REFERENCES

[1] T. Michal and J.-P. Eglizeaud, "GRAVES: The new french system for space surveillance," in *Proc. 4th European Conf. on Space Debris. ESA/ESOC.*, Darmstadt, Germany, 2005.

[2] H. Labriji, O. Herscovici-Schiller, and F. Cassaing, "Shadow imaging of geostationary satellites: Experimental demonstration with accurate polychromatic modelling of diffraction and atmospheric disturbances," in *Advanced Maui Optical and Space Surveillance Technologies Conference*, 2022. [Online]. Available: `https://amostech.com/TechnicalPapers/2022/Non-Resolved-Object-Characterization/Labriji.pdf`.

[3] K. Fujimoto, M. Uetsuhara, and T. Yanagisawa, "Statistical track-before-detect methods applied to faint optical observations of resident space objects," in *Advanced Maui Optical and Space Surveillance Technologies Conference*, 2015. [Online]. Available: `https://amostech.com/TechnicalPapers/2015/Orbital_Debris/Fujimoto.pdf`.

[4] T. S. Murphy, M. J. Holzinger, and B. Flewelling, "Visual tracking methods for improved sequential image-based object detection," *Journal of Guidance, Control, and Dynamics*, 2018. DOI: `10.2514/1.G002238`.

[5] M. Uetsuhara and N. Ikoma, "Faint debris detection by particle based track-before-detect method," in *Advanced Maui Optical and Space Surveillance Technologies Conference*, 2014. [Online]. Available: `https://amostech.com/TechnicalPapers/2014/Sensor_Processing/UETSUHARA.pdf`.

[6] S. Virani and D. M. Holzinger, "Real-time multi-target detection & tracking of space objects using FiSSt methods," in *Advanced Maui Optical and Space Surveillance Technologies Conference*, 2020.

[7] T. Delaite, D. S. Martinez, E. Glemet, *et al.*, "Détection au vol de cibles mobiles à faible rapport signal à bruit : Application à l'orbitographie.," in *28° Colloque sur le traitement du signal et des images*, Issue: 001-0307, Nancy: GRETSI - Groupe de Recherche en Traitement du Signal et des Images, 2022, p. 1229–1232.

[8] E. Pearce, J. A. Gregory, A. Smith, *et al.*, "Utilization of a curved focal surface array in a 3.5m wide field of view telescope," in *Advanced Maui Optical and Space Surveillance Technologies Conference*, 2013.

[9] M. Shao, B. Nemati, C. Zhai, *et al.*, "Finding very small near-earth asteroids using synthetic tracking," *The Astrophysical Journal*, vol. 782, 2014, ISSN: 0004-637X, 1538-4357. DOI: `10.1088/0004-637X/782/1/1`.

[10] M. Shao, R. Trahan, C. Zhai, *et al.*, "Synthetic tracking on a small telescope," in *Advanced Maui Optical and Space Surveillance Technologies Conference*, 2018.

[11] F. Cantalloube, D. Mouillet, L. M. Mugnier, *et al.*, "Direct exoplanet detection and characterization using the ANDROMEDA method: Performance on VLT/NaCo data," *Astronomy & Astrophysics*, vol. 582, A89, 2015, ISSN: 0004-6361, 1432-0746. DOI: `10.1051/0004-6361/201425571`.

[12] Gaia Collaboration, "The gaia mission," *Astronomy & Astrophysics*, vol. 595, A1, 2016, ISSN: 0004-6361, 1432-0746. DOI: 10.1051/0004-6361/201629272.

[13] "Gaia website." (), [Online]. Available: https://www.cosmos.esa.int/gaia.

[14] D. Lang, D. W. Hogg, K. Mierle, *et al.*, "Astrometry.net: Blind astrometric calibration of arbitrary astronomical images," *The Astronomical Journal*, 2010, ISSN: 0004-6256, 1538-3881. DOI: 10.1088/0004-6256/139/5/1782.

[15] D. Lang, D. W. Hogg, K. Mierle, *et al.* "Astrometry.net." (2012), [Online]. Available: http://astrometry.net (visited on 07/04/2022).

[16] J. Bangert, S. Bell, N. Capitaine, *et al.*, "SOFA astrometry tools," *Standards Of Fundamental Astronomy*, 2021. [Online]. Available: https://www.iausofa.org/sofa_ast_c.pdf.

[17] L. Prange, A. Villiger, D. Sidorov, *et al.*, "Overview of CODE's MGEX solution with the focus on galileo," *Advances in Space Research*, Scientific and Fundamental Aspects of GNSS - Part 1, vol. 66, no. 12, pp. 2786–2798, Dec. 15, 2020. DOI: 10.1016/j.asr.2020.04.038.

[18] J. Skuljan, "High-precision astrometric measurements of calibration satellites," in *Advanced Maui Optical and Space Surveillance Technologies Conference*, 2022.

[19] "Data processing and analysis consortium (DPAC) website." (), [Online]. Available: https://www.cosmos.esa.int/web/gaia/dpac/consortium.